



# *Novel heating/cooling stage designed for fluid inclusion microthermometry of large stalagmite sections*

Article

Accepted Version

Krüger, Y., Hiltbrunner, B., Luder, A., Fleitmann, D. and Frenz, M. (2014) Novel heating/cooling stage designed for fluid inclusion microthermometry of large stalagmite sections. *Chemical Geology*, 386. pp. 59-65. ISSN 0009-2541 doi: <https://doi.org/10.1016/j.chemgeo.2014.08.004> Available at <http://centaur.reading.ac.uk/40202/>

It is advisable to refer to the publisher's version if you intend to cite from the work.

Published version at: <http://dx.doi.org/10.1016/j.chemgeo.2014.08.004>

To link to this article DOI: <http://dx.doi.org/10.1016/j.chemgeo.2014.08.004>

Publisher: Elsevier

All outputs in CentAUR are protected by Intellectual Property Rights law, including copyright law. Copyright and IPR is retained by the creators or other copyright holders. Terms and conditions for use of this material are defined in the [End User Agreement](#).

[www.reading.ac.uk/centaur](http://www.reading.ac.uk/centaur)

## **CentAUR**

Central Archive at the University of Reading

Reading's research outputs online

# Novel heating/cooling stage designed for fluid inclusion microthermometry of large stalagmite sections

Yves Krüger<sup>1,4,\*</sup>, Beat Hiltbrunner<sup>2</sup>, Andres Luder<sup>1</sup>, Dominik Fleitmann<sup>3,4,5</sup>, Martin Frenz<sup>1</sup>

<sup>1</sup>Institute of Applied Physics, University of Bern, Switzerland

<sup>2</sup>Astronomical Institute, University of Bern, Switzerland

<sup>3</sup>Institute of Geological Sciences, University of Bern, Switzerland

<sup>4</sup>Oeschger Centre for Climate Change Research, University of Bern, Switzerland

<sup>5</sup>present address: Department of Archaeology, School of Archaeology, Geography and Environmental Sciences, University of Reading, United Kingdom

## Abstract

Liquid–vapour homogenisation temperatures of fluid inclusions in stalagmites are used for quantitative temperature reconstructions in paleoclimate research. Specifically for this application, we have developed a novel heating/cooling stage that can be operated with large stalagmite sections of up to  $17 \times 35 \text{ mm}^2$  to simplify and improve the chronological reconstruction of paleotemperature time-series. The stage is designed for use of an oil immersion objective and a high-NA condenser front lens to obtain high-resolution images for bubble radius measurements. The temperature accuracy of the stage is better than  $\pm 0.1 \text{ }^\circ\text{C}$  with a precision (reproducibility) of  $\pm 0.02 \text{ }^\circ\text{C}$ .

*Keywords:* microthermometry, heating stage, stalagmites, homogenisation temperature, paleotemperature

## 1. Introduction

During past decades stalagmites have become an important archive providing information on natural climate variations in the past (*e.g.* Fairchild *et al.*, 2006; Lachniet, 2009; McDermott *et al.*, 2004). Stalagmites can grow continuously over thousands of years by precipitation of calcite from the cave drip water and their age can precisely be dated using the uranium-series dating method. In weakly ventilated caves, the cave air temperature is nearly constant throughout the year and is closely related to the mean annual surface temperature outside the cave (Wigley and Brown, 1976). Thus, stalagmite formation temperatures can be used to develop time series of paleotemperature variations. In recent

---

\* corresponding author:

e-mail: [yves.krueger@iap.unibe.ch](mailto:yves.krueger@iap.unibe.ch)

phone: +41 (0)31 631 37 09

address: Sidlerstraße 5, CH-3012 Bern

Field Code Changed

35 years, different temperature proxies have been proposed to determine the formation  
36 temperatures of stalagmites: (i) the combination of  $\delta\text{D}$  and  $\delta^{18}\text{O}$  of fluid inclusion water and  
37 speleothem calcite, respectively (e.g. Schwarcz *et al.*, 1976; McGarry *et al.*, 2004; Vonhof *et*  
38 *al.*, 2006; Zhang *et al.*, 2008; Affolter *et al.*, 2014), (ii) the excess of  $^{13}\text{C}$ – $^{18}\text{O}$  containing  
39 molecules (so-called ‘clumped isotopes’) of calcite (Ghosh *et al.*, 2006; Affek *et al.*, 2008),  
40 and (iii) the concentration of dissolved noble gases in the fluid inclusion water (Kluge *et al.*,  
41 2008; Scheidegger *et al.*, 2010).

42 Recently, we have evaluated the applicability of fluid inclusion liquid–vapour  
43 homogenisation temperatures as an alternative approach to determine stalagmite formation  
44 temperatures (Krüger *et al.*, 2011). The method relies on the measurement of the temperature  
45 at which a two-phase liquid–vapour inclusion homogenises to a stable monophasic liquid state  
46 upon collapse of the vapour bubble. The temperature of the bubble collapse, i.e., the observed  
47 homogenisation temperature  $T_{h(obs)}$  depends on the density of the encapsulated drip water and  
48 on the volume of the fluid inclusion.  $T_{h(obs)}$  can be measured using a microscope  
49 heating/cooling stage. Prior to measuring liquid–vapour homogenisation temperatures in  
50 stalagmites, however, the initially monophasic liquid inclusions have to be transferred to a  
51 stable two-phase system by applying single ultra-short laser pulses to stimulate vapour bubble  
52 nucleation in the metastable liquid (Krüger *et al.*, 2007). Since stalagmites grow under  
53 atmospheric pressure conditions, the density of the water preserved in the inclusions depends  
54 only on the calcite formation temperature. By applying a thermodynamic model that accounts  
55 for the effect of surface tension on liquid–vapour homogenisation (Marti *et al.*, 2012) the  
56 density of the encapsulated drip water and hence the formation temperature of the stalagmite  
57 can be calculated based on the measurement of  $T_{h(obs)}$  and at least one additional measurement  
58 of the vapour bubble radius at a known temperature. Previous studies on recent fluid  
59 inclusions from the top part of actively growing stalagmites revealed a potential accuracy of  
60 this new temperature proxy of approximately  $\pm 0.2$  °C (Krüger *et al.*, 2011).

61

## 62 **2. Motivation to develop a novel heating/cooling stage**

63

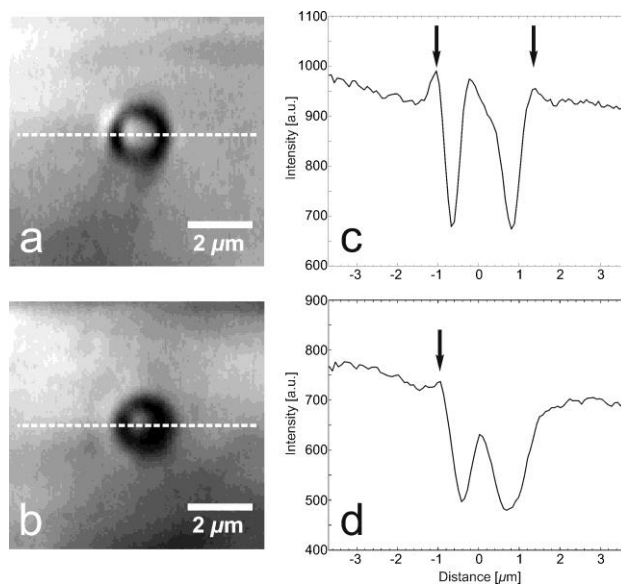
64 Fluid inclusions in stalagmites form during crystal growth (Kendall and Broughton,  
65 1978) and are typically arranged along calcite growth bands. Thus, the inclusions and the  
66 surrounding host calcite have the same age, which allows for a precise chronological  
67 reconstruction of stalagmite formation temperatures determined from fluid inclusions. In  
68 previous studies performed on a conventional Linkam THMSG 600 heating/freezing stage the

69 chronological reconstruction of the temperature data was complicated due to the fact that the  
70 maximum sample size is limited to 7 mm in diameter. Hence, the initially ca.  $20 \times 35 \text{ mm}^2$   
71 large and  $300\text{--}400 \text{ }\mu\text{m}$  thick stalagmite sections had to be broken into smaller pieces after  
72 removing them from the carrier glass that is needed to stabilize the sample during cutting.  
73 This means a considerable and time-consuming effort for sample documentation prior to  
74 microthermometric measurements. Nevertheless a precise reconstruction of the sections often  
75 failed when the sample fractured to tiny pieces upon dissolving the glue (cyanoacrylate) in an  
76 acetone bath. Therefore, the main motivation to build a new heating/cooling stage was to be  
77 able to examine entire stalagmite sections that no longer need to be removed from the carrier  
78 glass but remain fixed on a  $0.3 \text{ mm}$  thick glass substrate with  $28 \times 48 \text{ mm}^2$  standard  
79 dimensions.

80 The second reason to design a new stage was the application of a microscope objective and a  
81 condenser front lens with high numerical apertures (NA) to improve the optical resolution and  
82 the quality of the vapour bubble images that are used for determining the bubble radius  
83 (Spadin et al., in prep.). The bubble images are taken with a CCD camera at known sub-  
84 ambient temperatures: commonly at  $5.1 \text{ }^\circ\text{C}$ , when the bubble radius reaches its maximum  
85 (Marti et al., 2009). Since conventional heating/freezing stages like the Linkam THMSG 600  
86 allow for microthermometric measurements from  $-180$  up to  $600 \text{ }^\circ\text{C}$ , their design requires the  
87 application of long working distance (LWD) optics that, however, exhibit lower numerical  
88 apertures than objectives and condenser front lenses with short working distances. For  
89 example, the Olympus LMPlanFL 100x LWD objective we use for the Linkam stage has a  
90 NA of 0.8, while the condenser front lens with a working distance of approximately  $13 \text{ mm}$   
91 has a NA of approximately 0.4. For the new heating/cooling stage that was designed for  
92 applications in a narrow temperature range between  $-15$  and  $35 \text{ }^\circ\text{C}$ , we wanted to use a 1.3  
93 NA oil immersion objective (Olympus UPLFLN 100x) and a dry short working distance  
94 condenser front lens with a NA of 0.9. The application of an oil immersion objective suggests  
95 itself due to the fact that we do not polish the stalagmite sections but instead, we use  
96 immersion oil to reduce light scattering at the rough surfaces and thus make the sections  
97 transparent for microscopic observations in transmission. To illustrate the improvements of  
98 the image quality and resolution, Fig. 1 shows a comparison of two microphotographs of the  
99 same vapour bubble taken with the new (Fig. 1a) and the old (Fig. 1b) system. In Fig. 1a the  
100 bubble image shows a dark ring with high contrast, whereas in Fig. 1b the dark ring appears  
101 much broader and blurred due to lower contrast. Based on a simple ray-tracing model, Spadin  
102 et al. (in prep.) found that reflection of light at the bubble meniscus results in a bright ring

103 surrounding the dark one. The intensity of this bright ring depends on the NA of the objective,  
104 which is illustrated in Fig. 1c for the oil immersion objective (NA 1.3) and in Fig. 1d for the  
105 LWD objective (NA 0.8). The intensity profile in Fig. 1c displays two distinct intensity  
106 maxima outside the dark ring, whereas in Fig. 1d the two peaks can hardly be distinguished  
107 from the background. In Fig. 1a and 1b the bright outer ring is only partially visible, which is  
108 likely due to shadow effects occurring in the stalagmite section and resulting in a non-uniform  
109 illumination of the vapour bubble.

110 An additional advantage of the oil immersion objective compared to the LWD objective is the  
111 smaller focal spot size due to the higher numerical aperture and a significantly higher  
112 transmission of the 800 nm laser wavelength emitted from the Ti:sapphire femtosecond (fs)  
113 laser that is used to induce bubble nucleation. This means that for a given energy and duration  
114 of the fs-laser pulse, the oil immersion objective provides a much higher pulse intensity in the  
115 focus than the LWD objective, and in consequence, allows us to induce vapour bubble  
116 nucleation in inclusions that are located up to 250  $\mu\text{m}$  below the sample surface.



117  
118 Fig. 1: Comparison of bubble images: a) microphotograph using a 100x oil immersion  
119 objective (NA 1.3) and a condenser NA of 0.9. b) microphotograph using a 100x LWD  
120 objective (NA 0.8) and a condenser NA of 0.4. c) and d) intensity profiles along the dashed  
121 lines indicated in a) and b). Arrows indicate the intensity maximum of the outer bright ring.  
122

### 123 3. Design of the heating/cooling stage

124

125 In the following we describe the design of the novel heating/cooling stage that is

126 illustrated in Fig. 2a–e. All components described in the text are labelled in the figures  
127 accordingly. The heating/cooling stage is mounted on a Olympus BX51 microscope (Fig. 2c)  
128 and its dimensioning complies with the requirements set by the large sample size and the  
129 short working distances of the microscope optics. To meet these demands we constructed a  
130 large-sized ( $\varnothing$  116 mm) heating/cooling block (A) made from copper, a material with  
131 excellent thermal conductivity. The rear side of this copper block features a central recess to  
132 bring the condenser front lens (C) close to the sample (Fig. 2b). The sample (III) is placed on  
133 the top face of the block (Fig. 2a). The 0.9 NA condenser front lens used has a working  
134 distance of  $\sim$ 3.5 mm and illuminates the sample through a tapered aperture with a final  
135 diameter of 1.5 mm (Fig. 2b). The heating/cooling block (A) comprises (i) a sheathed twin-  
136 core heating conductor (1; Thermocoax) of 1.7 m length and a diameter of 1.5 mm, which is  
137 soldered in a spirally routed groove closely below to the surface (Fig. 2b); (ii) a cooling unit  
138 (II) consisting of a cooling circuit (2) with inlet and outlet connections for the cooling liquid,  
139 a water-ethylene glycol mixture. The cooling unit is placed below the heating conductor; (iii)  
140 a Pt-100 thin-film temperature sensor (3; Heraeus) embedded in a slot on the top face of the  
141 copper block (Fig. 2a).

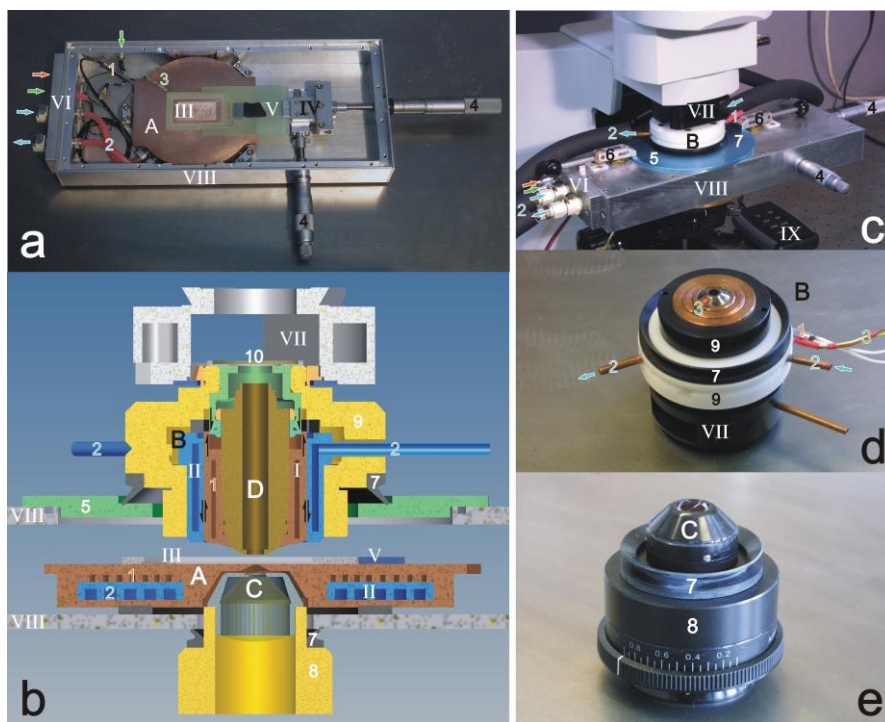
142 The sample (III), i.e., the 0.3 mm carrier glass with the stalagmite section, is fixed in a 2 mm  
143 thick fibreglass frame that prevents leakage of the immersion oil on the copper block (Fig.  
144 2a). For the preparation of the sample we use UV curable epoxy resins that are inert against  
145 the immersion oil and can be applied at sub-ambient temperatures. Prior to the cutting of the  
146 sections, the stalagmite sample is fixed on the carrier glass using a low-viscous resin (Epo-  
147 Tek OG603) that closely matches the refractive index of calcite ( $n_e = 1.486$ ) in the cured state.  
148 The carrier glass is then fixed to the bottom side of the fibreglass frame using a different,  
149 higher viscous resin (Epo-Tek OG142). The fibreglass frame can be magnetically attached to  
150 the sample holder (V) that is mounted on an x-y translation stage (IV). The translation stage is  
151 moved by means of two micrometre gauges (4) with travel lengths of 50 mm and 25 mm,  
152 respectively. The position of the sample can be read off from the scales on the micrometre  
153 gauges, which allows for a precise localisation of the analysed fluid inclusions mandatory for  
154 the chronological reconstruction of the temperature data. The maximum size of the stalagmite  
155 sections that can be scanned with the oil immersion objective is  $17 \times 35 \text{ mm}^2$ .

156 The application of an immersion objective (D) that is in direct thermal contact with the  
157 oil film covering the stalagmite sample requires an active control of the objective temperature  
158 to minimise vertical temperature gradients and to achieve faster equilibration of the sample  
159 temperature. Therefore, we have developed a copper heating/cooling jacket (B) that allows for

160 a precise regulation of the objective temperature. To accomplish an efficient heat transfer, the  
161 heating/cooling jacket is attached directly to the inner brass cylinder that houses the objective  
162 lenses (D). To this end, we removed the outer protective sleeve of the objective and modified  
163 the spring system that protects the front lens from mechanical damage. The cylindrical  
164 heating/cooling jacket consists of a heater element (I) that is made up of a coiled twin-core  
165 heating conductor (1) embedded between two copper sleeves and an outer cooling unit (II)  
166 with inlet and outlet connections (2) for the cooling liquid. The heater element (I) is screwed  
167 on the objective (D) and features a 2 mm spring deflection relative to the cylindrical cooling  
168 unit (II) that serves as guidance for the spring suspension of the objective. An insulating  
169 sheath (9) made from Polyoxymethylene (POM), finally, encases the heating/cooling jacket.  
170 The back aperture of the POM sheath is sealed with a 1 mm glass window (10) to prevent  
171 condensation of moisture on the objective rear lens and within the heating/cooling jacket. The  
172 whole assembly is fixed to the microscope frame by means of a detachable single-position  
173 nosepiece (VII) with centring screws to align the objective to the optical axis. A lateral  
174 through-hole (11, Fig. 2d) in the nosepiece can be used to flush the glass window with  
175 nitrogen gas to remove the condensed air moisture from the glass window. The objective  
176 temperature, finally, is measured by a Pt-100 thin-film sensor (3) that is placed close to the  
177 objective front lens (Fig. 2d).

178 The sample chamber is placed inside a sealed off aluminium housing (VIII) to  
179 minimise condensation of air moisture and thermal effects induced by air circulation. An  
180 opening in the base plate ( $\varnothing$  34 mm) provides access to enter the condenser front lens (C) and  
181 is sealed off by a V-seal (7) mounted on the outer face of the adapter tube (8) that tightly  
182 connects the aperture diaphragm and the front lens of the condenser (Fig. 2e). From above,  
183 the objective with the heating/cooling jacket can be entered through an opening ( $\varnothing$  60 mm) in  
184 the centre of the detachable cover plate (5). A V-seal (7) mounted on the POM insulation  
185 sheath seals off the port when the objective comes close to the sample. The cover plate is  
186 fixed to the housing by means of two clamping levers (6) and thus can be easily and quickly  
187 removed to load the sample. Finally, a plug board (VI) in the side wall of the aluminium  
188 housing is used as lead-through to connect the lower heating/cooling block (A) to the electric  
189 and the hydraulic circuits (Fig. 2a,c).





190  
191  
192  
193  
194

Fig. 2: a) View of the heating/cooling stage with removed cover b) Cross-section through the stage and the objective heating/cooling jacket c) stage mounted on the microscope d) objective with heating/cooling jacket e) condenser assembly.

195

Legend:

196

A: heating/cooling block B: objective heating/cooling jacket C: condenser lens D: oil immersion objective.

197

I: heater element II: cooling element III: sample IV: x-y translation stage V: sample holder VI: plug board VII: objective nose piece VIII: stage housing IX: remote control.

198

1: heating conductors 2: cooling circuits 3: Pt-100 sensors 4: micrometer gauge 5: detachable cover plate 6: clamping lever 7: V-seal 8: adapter tube 9: insulating sheath 10: window 11:gas inlet

199

Connections are indicated by arrows: red for heating conductor, blue for cooling circuit, green for Pt-100 sensor and grey for nitrogen gas.

200

201

202

#### 4. Mode of operation of the stage

203

204

205

206

207

The twin-core heating conductors (1) in the lower copper block (A) and in the objective jacket (B) are connected to separate power supply units (Elektro Automatik EA-PS 3150-04 B) to enable independent temperature control of the two heating/cooling elements. A cryo-thermostat (Lauda ProLine RP 845) is used to feed the two cooling circuits and provides for a constant temperature and flow rate of the cooling liquid. The stage is operated under permanent circulation of the coolant, while the temperature of the two heating/cooling

208

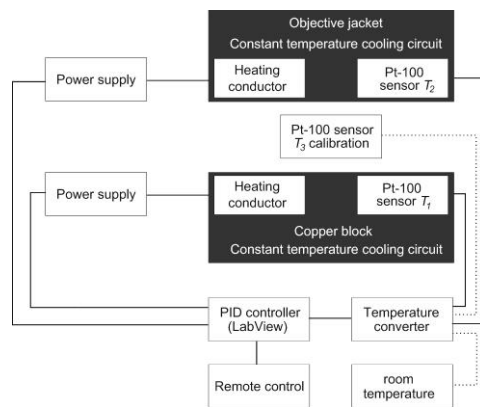
209

210

211

212

213 elements is regulated individually by varying the voltage impressed on the heating  
 214 conductors. The stage reaches a maximum sample temperature that is 50°C in excess of the  
 215 coolant temperature set at the thermostat. Considering the specific application to fluid  
 216 inclusions in stalagmites and the use of immersion oil, a 50 °C temperature range of the stage  
 217 is more than sufficient. The two Pt-100 sensors (3) attached to the lower heating/cooling  
 218 block and to the microscope objective, respectively, are connected to a four-channel  
 219 temperature converter (National Instruments). The temperature converter and the two power  
 220 supply units are connected to a computer via USB interfaces. A LabView® based PID  
 221 (Proportional-Integral-Derivative) controller is used to regulate the temperature of the two  
 222 heating/cooling elements. For convenience, the stage can be operated via the function keys of  
 223 a remote control (IX, Fig. 2c). A flow chart of the temperature control system is shown in Fig.  
 224 3.



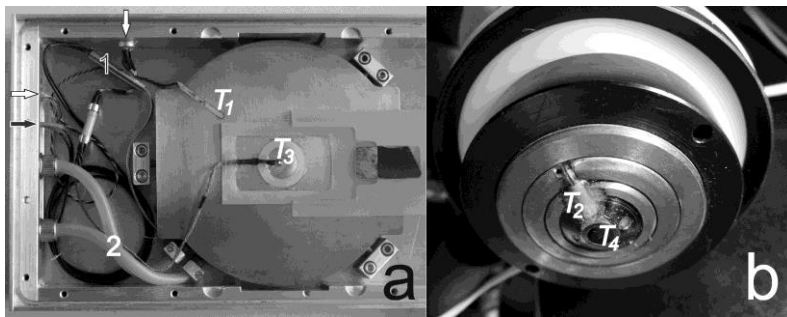
226  
 227  
 228 Fig. 3: Scheme of the temperature control of the heating/cooling stage. For the calibration of the stage additional  
 229 Pt-100 sensors can be connected to measure the sample temperature and to monitor room temperature variations  
 230 (see section below)

231  
 232  
 233  
 234

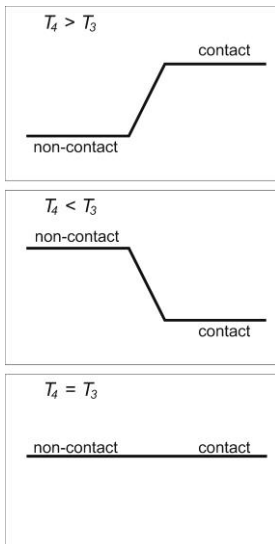
### 5. Thermal characterisation and temperature calibration of the stage

235 To characterise the thermal properties of the heating cooling stage such as precision,  
 236 accuracy and equilibration times, we used an additional Pt-100 thin-film sensor fixed on a  
 237 0.3 mm glass substrate and embedded in epoxy resin (Fig. 4a). This sensor allows us to  
 238 measure the sample temperature ( $T_3$ ) in the centre of the lower copper block, i.e., in the  
 239 optical path of the microscope. The regular Pt-100 sensor ( $T_1$ ) embedded in the lower copper  
 240 block is about 40 mm off the centre, which means that  $T_3$  is not equal  $T_1$  due to lateral thermal  
 241 gradients. The same applies for the objective temperature  $T_2$  that is not equal to the

242 temperature of the front lens  $T_4$  (Fig 4b). Since we cannot directly measure the sample and  
 243 front lens temperatures during fluid inclusion microthermometry, we need a calibration to  
 244 determine  $T_3$  and  $T_4$  based on the two set temperatures  $T_1$  and  $T_2$ . Furthermore,  $T_4$  should  
 245 equal  $T_3$  to avoid vertical temperature gradients within the sample. We recall that the  
 246 objective front lens is in contact with sample via the immersion oil. The PID controller is  
 247 capable of holding  $T_1$  and  $T_2$  constant within  $\pm 0.01$  °C, which determines the fluctuation of  $T_3$   
 248 and  $T_4$ .  
 249



250  
 251  
 252 Fig. 4: Positions of temperature measurements for the stage calibration. a)  $T_1$ : surface temperature of the copper  
 253 block 40 mm apart from the sample position, measured with a permanent Pt-100 sensor.  $T_3$ : sample temperature  
 254 measured with an additional Pt-100 sensor used only for calibration. b)  $T_2$ : objective temperature close to the  
 255 front lens measured with a permanent Pt-100 sensor.  $T_4$ : temperature of the objective front lens, not measured  
 256 directly (see text for details).  
 257



258  
 259  
 260 Fig. 5: Schematic representation of the measurement procedure used to calibrate of the objective front lens  
 261 temperature  $T_4$  by minimising the temperature gradient between  $T_3$  and  $T_4$  (see text for details)  
 262

263 For the calibration of the stage it was not practicable to measure both the front lens  
264 temperature  $T_4$  and the sample temperature  $T_3$  independently. Instead of measuring  $T_4$   
265 directly, we only measured  $T_3$  as a function of  $T_1$  and minimised the vertical temperature  
266 gradient between  $T_3$  and  $T_4$  by adjusting the objective set temperature  $T_2$ . In practice, we  
267 measured  $T_3$ , first, in a non-contact configuration with the objective front lens about 0.3 mm  
268 above the immersion oil covering the embedded Pt-100 sensor and, subsequently, in a contact  
269 configuration with the front lens immersed in the oil and thus in thermal contact with the Pt-  
270 100 sensor. In this way, we were able to detect thermal gradients between the objective front  
271 lens and the sample (Pt-100 sensor) on the basis of the temperature change of  $T_3$ . By adjusting  
272 the objective set temperature  $T_2$  in repeated measurements, we finally minimised the thermal  
273 gradients and thus the change of  $T_3$  when switching over to the contact configuration. This  
274 calibration procedure is illustrated schematically in Fig. 5. Calibration measurements were  
275 performed at different sample temperatures  $T_3$  and for different coolant temperatures  $T_{coolant}$ .  
276 The results are shown in Fig. 6. The diagram displays the deviation of the two set  
277 temperatures,  $T_1$  and  $T_2$ , from the calibrated sample temperature  $T_{3(cal)}$  ( $\Delta T_{set} = T_{set} - T_{3(cal)}$ ) as  
278 function of  $T_{3(cal)}$  for coolant temperatures of 0, -5, -10 and -15 °C. The relation between  
279  $\Delta T_{set}$  and  $T_{3(cal)}$  is nearly linear for both, the lower copper block ( $T_1$ ) and the objective ( $T_2$ ). To  
280 test our calibration, we repeated the measurements of the sample temperature in the contact  
281 configuration. Measurements were taken in 5 °C increments using a heating/cooling rate of 5  
282 °C/min and an equilibration time of 15 minutes after each temperature step. Fig. 7 illustrates  
283 that the deviation of the measured sample temperatures  $T_{3(meas)}$  from the calibration  
284 temperature  $T_{3(cal)}$  is less than  $\pm 0.02$  °C, except for some measurements performed with a  
285 coolant temperature of -15 °C, which show a slightly larger deviations above 15 °C. This is  
286 due to the limited cooling capacity of the thermostat, which results in a slight increase of  
287  $T_{coolant}$  with increasing stage temperature and larger temperature fluctuations. In addition, Fig.  
288 7 indicates a small hysteresis between heating and cooling runs. Repeated measurements with  
289 the same coolant temperature yield a precision (reproducibility) of  $T_3$  of  $\pm 0.01$  °C.

290 The temperature tolerance of the Pt-100 sensors ( $1/3$  Class B) used for the calibration is  
291  $\pm 0.1$  °C at 0 °C and  $\pm 0.15$  °C at 30 °C. To further improve the accuracy of the sample  
292 temperature  $T_3$  below  $\pm 0.1$  °C, we used synthetic H<sub>2</sub>O and H<sub>2</sub>O-CO<sub>2</sub> fluid inclusions for  
293 absolute temperature calibrations. The use of synthetic fluid inclusions allows us to compare  
294 our measurements with well-known reference temperatures, namely the melting temperature  
295 of ice at 0.0 °C and the critical homogenisation of CO<sub>2</sub> in the H<sub>2</sub>O- CO<sub>2</sub> system at 31.42 °C  
296 (Morrison 1981). Measurements were performed with different coolant temperatures yielding

297 a precision of  $\pm 0.02$  °C and a slight offset of  $T_3$  to lower temperatures:  $-0.1$  ° at  $0.0$  °C and –  
 298  $0.15$  ° at  $31.42$  °C. Using these offset values for a correction of the calibration, we can  
 299 achieve a temperature accuracy of the heating/cooling stage of approximately  $\pm 0.05$  °C.  
 300

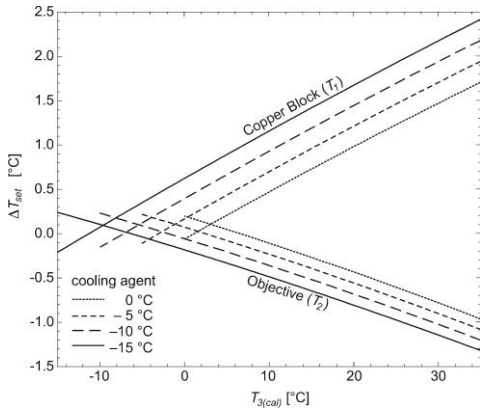


Fig 6: Deviation of the set temperatures  $T_1$  and  $T_2$  from the calibrated sample temperature  $T_{3(cal)}$  for different coolant temperatures indicated by colours (see text for details).

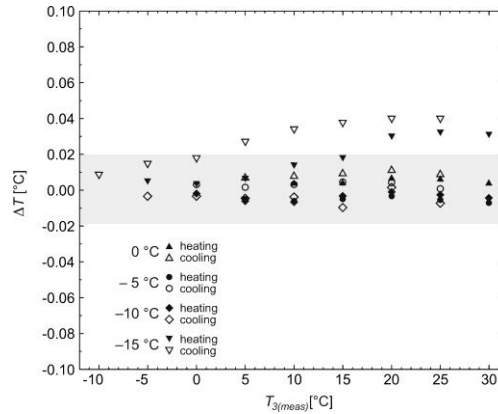


Fig. 7: Calibration check illustrating the deviation of the measured sample temperature value  $T_{3(meas)}$  from the calibration  $T_{3(cal)}$ . Filled symbols denote measurements upon heating, open symbols upon cooling. Colours indicate different coolant temperatures.

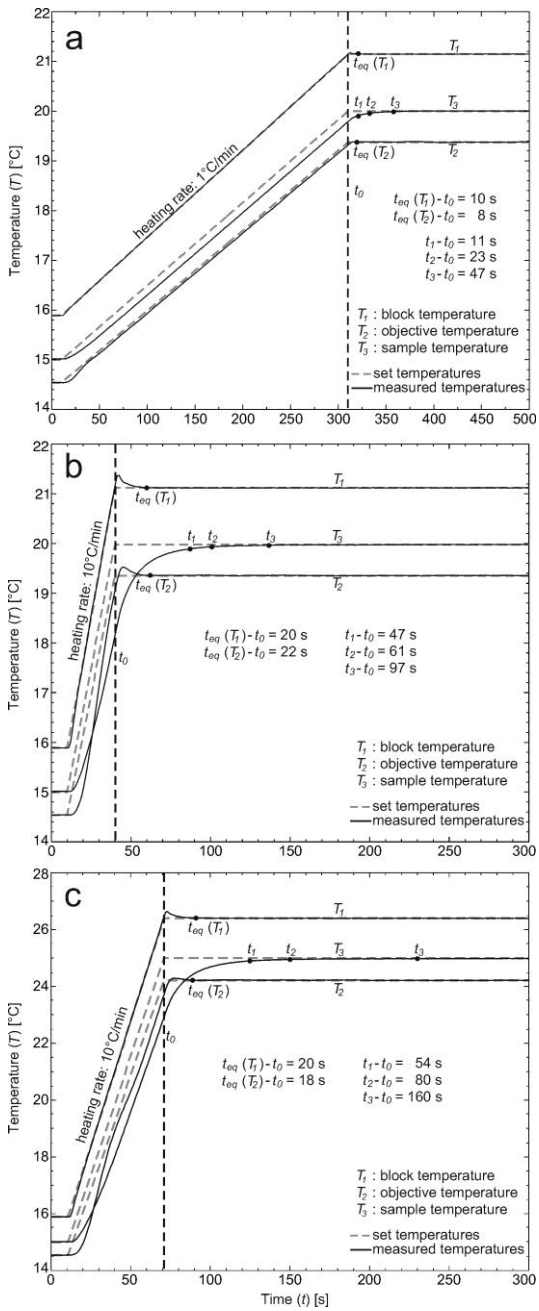
301  
 302 The measurements of the ice melting temperature have also shown that absorption of  
 303 light in the sample can increase  $T_3$  by up to  $0.05$  °C, in spite of using a heat-absorbing IR-  
 304 filter (Schott KG5 IR) in the illumination light path. In consequence of the absorption the  
 305 effective sample temperature is higher than predicted by the calibration, which results in an  
 306 underestimation of the ice melting temperature. To deal with this potential uncertainty we are  
 307 working with a pre-defined setting of the light intensity and of the field diaphragm for sample  
 308 illumination. Finally, we investigated the effect of room temperature fluctuations on the  
 309 sample temperature. Both  $T_3$  and the room temperature were measured with Pt-100 sensors.  
 310 The results of these measurements indicate that a change in room temperature of  $1$  °C affects  
 311 the sample temperature by less than  $0.01$  °C, which is a negligible error in an air-conditioned  
 312 lab with room temperature fluctuations of less than  $\pm 2$  °C.

313 Besides precision and accuracy we also analysed the dynamic properties of the stage,  
 314 namely the temperature equilibration times. The equilibration time  $t_{eq}$  denotes the time lag of  
 315 the system to reach a stable temperature state after a temperature change  $\Delta T$ . The time at  
 316 which the set temperature reaches its new value serves as reference time  $t_0$ . Equilibration  
 317 times were measured for  $T_1$ , the temperature of the lower heating/cooling block, for  $T_2$ , the

318 objective temperature and for the sample temperature  $T_3$ . Figure 8 illustrates the nominal  
319 (dashed lines) and the measured temperature trends (solid lines) of  $T_1$ ,  $T_2$  and  $T_3$  as a function  
320 of time for different temperature changes  $\Delta T$  and heating rates. The diagrams show that  $T_1$   
321 and  $T_2$  slightly over-shoot the set temperatures after heating is stopped and then return to their  
322 set values. The equilibration times  $t_{eq}$  of  $T_1$  and  $T_2$  are very similar and depend only on the  
323 heating rate (~10 s at 1 °C/min, ~20 s at 10 °C/min). The sample temperature  $T_3$ , in contrast,  
324 approaches its set temperature asymptotically from below with a considerable time lag. The  
325 time the system needs to reach a stable sample temperature is too long for practical use (up to  
326 360 seconds) and therefore we defined three time markers  $t_1$ ,  $t_2$  and  $t_3$  at which the sample  
327 temperature is 0.1, 0.05 and 0.02 °C, respectively, below the final sample temperature  $T_3(eq)$ .  
328 Fig. 8 shows that  $t_1$ ,  $t_2$  and  $t_3$  depend on the heating rate as well as on the temperature change  
329  $\Delta T$ . With respect to fluid inclusion measurements  $t_1$  implies a temperature overestimation of  
330 0.1 °C,  $t_2$  of 0.05 °C and  $t_3$  of 0.02 °C. This means that the accuracy of the  $T_h$  measurements  
331 also depends on the measuring routine that needs to be adjusted accordingly.

332 In practise, we use a rate of 10 °C/min to heat the stage to a temperature that is  
333 approximately 2–3 °C below the expected homogenisation temperature. After an equilibration  
334 time of 60-90 seconds, further heating is accomplished with a rate of 1 °C/min. Close to the  
335 homogenisation, finally, when the vapour bubble becomes very small, the temperature is  
336 increased stepwise in 0.05 °C increments until  $T_h$  is reached. During this last phase of the  
337 measurement the sample temperature closely follows the set temperature.

338  
339



340  
 341  
 342 Fig. 8: Temperature-time plots illustrating the equilibration times of  $T_1$ ,  $T_2$  and  $T_3$  after temperature increases: a)  
 343 5 °C at a heating rate of 1 °C/min b) 5 °C at a heating rate of 10° C/min and c) 10 °C at a heating rate of  
 344 10 °C/min. Dashed lines indicate the set temperatures and solid lines represent the measured temperature trends.  
 345 The reference time  $t_0$  denotes the end of the heat-up phase (dashed vertical line).  
 346  
 347

348  
349  
350  
351  
352  
353  
354  
355  
356  
357  
358  
359  
360  
361  
362  
363  
364  
365  
366  
367  
368  
369  
370  
371  
372  
373  
374  
375  
376  
377  
378  
379  
380  
381  
382  
383  
384  
385  
386  
387  
388  
389  
390

## 6. Conclusions

Liquid–vapour homogenisation of fluid inclusions in stalagmites is a promising new approach to accurately reconstruct paleotemperature variations with high temporal resolution. For this specific application, we have developed a novel heating/cooling stage for operation with large stalagmite sections and high-NA optics. With a temperature accuracy well below  $\pm 0.1$  °C and a precision of  $\pm 0.02$  °C the stage meets the requirements for fluid inclusion measurements in this temperature range. In a next step of development we will factor the dynamic properties of the stage into the PID temperature control to further reduce the equilibration times after large temperature changes and thus, to increase the efficiency of the  $T_h$  measurements.

## Acknowledgements

The authors thank N. Jaussi, A. Jenk and A. Friedrich for manufacturing the components of the stage and for helpful discussions.

This work is part of the SINERGIA project “*STALCLIM – Multi-proxy climatic and environmental reconstructions from stalagmites from Switzerland, Turkey, Arabia and India*” (SNF grant: CSRI22–132646/1)

## References:

- Affek, H. P., Bar-Matthews, M., Ayalon, A., Matthews, A., and Eiler, J. M., 2008. Glacial/interglacial temperature variations in Soreq cave speleothems as recorded by ‘clumped isotope’ thermometry. *Geochim. Cosmochim. Ac.*, 72, 5351-5360.
- Affolter, S., Fleitmann, D., and Leuenberger, M., 2014. New on-line method for water isotope analysis of speleothem fluid inclusions using laser absorption spectroscopy (WS-CRDS). *Clim. Past Discuss.*, 10, 429-467,
- Fairchild, I.J., Smith, C.L., Baker, A., Fuller, L., Spötl, C., Matthey, D. and McDermott, F., 2006. Modification and preservation of environmental signals in speleothems. *Earth Sci. Rev.* 75, 105-153.
- Ghosh, P., Adkins, J., Affek, H., Balta, B., Guo, W., Schauble, E.A., Schrag, D., and Eiler, J.M., 2006.  $^{13}\text{C}$ - $^{18}\text{O}$  bonds in carbonate minerals: A new kind of paleothermometer. *Geochim. Cosmochim. Ac.*, 70, 1439-1456.
- Kendall, A. C. and Broughton, P. L., 1978. Origin of Fabrics in Speleothems Composed of Columnar Calcite Crystals. *J. Sediment. Petrol.*, 48, 519-538.

Formatted: German  
(Switzerland)

Formatted: German  
(Switzerland)



- 391 Kluge, T., Marx, T., Scholz, D., Niggemann, S., Mangini, A., and Aeschbach-Hertig, W., 2008. A new tool for  
392 palaeoclimate reconstruction: Noble gas temperatures from fluid inclusions in speleothems. *Earth Planet. Sc.*  
393 *Lett.*, 269, 407-414.  
394
- 395 Krüger, Y., Stoller, P., Rička, J., and Frenz, M., 2007. Femtosecond lasers in fluid-inclusion analysis:  
396 overcoming metastable phase states. *Eur. J. Mineral.*, 19, 693-706.  
397
- 398 Krüger, Y., Marti, D., Hidalgo Staub, R., Fleitmann, D., and Frenz, M., 2011. Liquid-vapour homogenisation  
399 of fluid inclusions in stalagmites. Evaluation of a new thermometer for paleoclimate research: *Chem. Geol.*, 289,  
400 39-47.  
401
- 402 Lachniet, M.S., 2009. Climatic and environmental controls on speleothem oxygen-isotope values. *Quaternary*  
403 *Sci. Rev.*, 28(5-6), 412-432.  
404
- 405 Marti, D., Krüger, Y., Frenz, M., 2009: Fluid inclusion liquid-vapour homogenization in the vicinity of the  
406 density maximum of aqueous solutions. *ECROFI XX Abstract*  
407
- 408 Marti, D., Krüger, Y., Fleitman, D., Frenz, M., and Rička, J., 2012. The effect of surface tension on liquid-gas  
409 equilibria in isochoric systems and its application to fluid inclusions. *Fluid Phase Equilib.*, 314, 13-21.  
410
- 411 McDermott, F., 2004. Palaeo-climate reconstruction from stable isotope variations in speleothems: a review.  
412 *Quaternary Sci. Rev.*, 23, 901-918.  
413
- 414 McGarry, S., Bar-Matthews, M., Matthews, A., Vaks, A., Schilman, B. and Ayalon, A., 2004. Constraints on  
415 hydrological and paleotemperature variations in the Eastern Mediterranean region in the last 140 ka  
416 given by the delta D values of speleothem fluid inclusions. *Quaternary Sci. Rev.*, 23, 919-934.  
417
- 418 Morrison, G., 1981. Effect of water upon the critical points of carbon dioxide and ethane. *J. Phys. Chem.*, 85:  
419 759-761.  
420
- 421 Scheidegger, Y., Baur, H., Brennwald, M.S., Fleitmann, D., Wieler, R., Kipfer, R., 2010. Accurate analysis of  
422 noble gas concentrations in small water samples and its application to fluid inclusions in stalagmites. *Chem.*  
423 *Geol.*, 272, 31-39.  
424
- 425 Schwarcz, H.P., Harmon, R.S., Thompson, P., Ford, D.C., 1976. Stable isotope studies of fluid inclusions in  
426 speleothems and their paleoclimatic significance. *Geochim. Cosmochim. Ac.*, 40, 657-665.  
427
- 428 Spadin, F., Marti, D., Hidalgo Staub, R., Krüger, Y., Rička, J., Fleitmann, D., Frenz, M., *in prep.* Accuracy of  
429 stalagmite formation temperatures determined from vapour bubble radius measurements in fluid inclusions.  
430
- 431 Vonhof, H.B., van Breukelen, M.R., Postma, O., Rowe, P.J., Atkinson, T.C., Kroon, D., 2006. A continuous-  
432 flow crushing device for on-line  $^7\text{Mg}$  analysis of fluid inclusion water in speleothems. *Rapid Commun. Mass*  
433 *Sp.*, 20, 2553-2558.  
434
- 435 Wigley T.M.L. & Brown M.C., 1976 - The physics of caves. In: Ford T.D. & Cullingford C.H.D. (Eds.), *The*  
436 *Science of Speleology*. New York: Academic Press: 329-358.  
437
- 438 Zhang, R., Schwarcz, H. P., Ford, D. C., Schroeder, F. S., and Beddows, P. A., 2008. An absolute  
439 paleotemperature record from 10 to 6 Ka inferred from fluid inclusion D/H ratios of a stalagmite from  
440 Vancouver Island, British Columbia, Canada. *Geochim. Cosmochim. Ac.*, 72, 1014-1026.

Formatted: German  
(Switzerland)